Lab 06: Inorganic Scintillation Detectors
Ceser Zambrano
NPRE 451
Gregory Romanchek
Md Fazlul Huq
Dr. Ming Fang
Dr. Angela Di Fulvio
22 March 2024

Table of Contents

Abstract

Introduction and Background

For this lab, we want to acquire gamma-ray energy spectra for multiple sources using a thallium-activated sodium iodide (NaI (TI)) scintillation device. We'll investigate and characterize gamma-ray interactions with matter. Additionally, we'll determine the composition of an unknown gamma-ray emitting isotope. Furthermore, we'll characterize the energy resolution of the NaI (TI) detector used. Finally, we'll conduct a series of attenuation experiments to determine the gamma-ray attenuation coefficients for three different materials.

Inorganic Scintillator Basics

Scintillators are materials that produce sparks of light when ionizing radiation interacts with them. The emitted light is small, however, needing to be amplified before a pulse can be recorded. To accomplish this, photomultiplier tubes are used to amplify the emitted light to a strong pulse for detection. Three types of scintillators are used for radiation detection: organic, inorganic, and gaseous. However, this lab only inorganic scintillators.

Inorganic scintillators (or detectors) are usually in the form of crystals of different alkali metals with some impurity. Inorganic detectors such as the thallium-activated sodium-iodide

crystal (NaI (TI)) are used for gamma-ray detection due to their high density. Inorganic detectors tend to have better light output but also have slow response time. Furthermore, inorganic detectors are hygroscopic and fragile, meaning extreme containment and care must be followed when dealing with these detectors.

Inorganic scintillators work in a complicated manner, as described above. On entering the detector crystal, the impinging photon will cause ionization, allowing free electrons to recombine in the crystal lattice. Upon recombination, heat and vibrations are produced and the activator emits light. This light emission is transparent to crystal, allowing for some light to the photocathode of the photomultiplier (PM) tube. This impinging light causes electron emission, which are then collected on the first dynode of the PM tube. This collection of electrons results in a charge buildup, which is then multiplied and sent towards the next dynode. This process occurs depending on the number of dynodes in the PM tube, culminating in a signal wire collecting these electrons and producing a detector signal. This signal is proportional to the energy of the incident gamma-ray, allowing for accurate energy measurements to be made using an inorganic scintillator. These signals can be sent to a multi-channel analyzer and displayed for data analyzation.

Detection and Gamma-Ray Interactions in Matter

When dealing detecting gamma-rays, it's not safe to assume that mono-energetic gamma-rays will produce signals of the same amplitude. Furthermore, the distribution of these signals will not be constant. Multiple factors influence this behavior such as the direction-dependent energy deposition of detector, statistical variation in the number of signal carriers, and the number of energy depositions that occur on the detector. Of the mentioned processes, gamma-ray interactions with matter impact the distribution and amplitude of these signals. The photoelectric effect,

Compton scattering, and pair production all have impacts on the gamma-ray energy spectra as impinging gamma-rays are detected.

The photoelectric effect occurs for low photon energies primarily. In this interaction type, a gamma-ray interacts with an atom and using all its energy to liberate a bound inner-shell electron and impart some kinetic energy on it. This freed inner-shell electron is set out of the atom and another electron will take its place, emitting X-rays and Auger electrons. For radiation detection, the energy of the liberated electron and the energy of emitted X-ray are detected and reported in the gamma-ray spectrum.

The second interaction, Compton scattering, occurs at intermediate gamma-ray energies. Compton scattering is the collision between a gamma-ray and outer-shell electron, resulting in scattering of both electrons and gamma-rays at different energies than what they had at the beginning of the interaction. This gamma-ray interaction depends on the incident energy of the gamma-ray and the scattering angle of the gamma-ray. Additionally, the scattered electron is also dependent on these factors, impacting its energy after the collision. Therefore, for different resulting scattering angles, we can expect to see a distribution of the electron energy as the scattering angle is increased from 0-degrees. The empirical formulation for Compton scattering kinematics for both scattered gamma-ray and electron is given by the following equations:

$$E'_\gamma = \frac{E_\gamma}{1 + \frac{E_\gamma}{m_e c^2}(1 - \cos(\theta))}$$

$$E_e = E_\gamma - E'_\gamma \qquad (1)$$

where E_e and E'_γ are the scattered electron and gamma-ray energy, respectively; E_γ is the initial energy of the gamma-ray, $m_e c^2$ is the rest mass energy of the electron, and θ is the scattering angle the gamma ray scatters with. For detection, the location at which this interaction is important to

consider. In the case that the gamma-ray undergoes Compton interactions near the edge of the detector, it's expected that the scattered gamma-ray leaves the detector and only the scattered electron is detected. This event results in a Compton distribution, covering the entire range of energy that electrons can have. The end of this distribution is described as the Compton edge or the maximum energy that an electron can have after a direct hit from a gamma-ray. Following a direct hit Compton interaction or a gamma-ray interaction with the material surrounding the detector, a visible peak corresponding to the minimum energy that a scattered photon can have.

The third possible interaction is pair production and occurs at gamma-ray energies greater than 1022 keV. Pair production involves a high-energy gamma-ray spontaneously converting its energy into producing an electron and positron. Each particle has an energy of 511 keV. For detection consideration, the production of the electron and positron are mainly focused on. After their creation and eventual propagation through material, they slow down through energy loss mechanisms. As soon as the positron reaches a slow enough speed, it will annihilate and produce two 511 keV annihilation gamma-rays. These gamma-rays are crucial for characterizing pair production, seeing as though either one or both annihilation gamma-rays can escape the detector. If both annihilation gamma-rays are detected, the signal produced will correspond to the full energy of the incident gamma-ray. If one gamma-ray escapes, the signal produced will correspond to approximately full energy of the incident gamma-ray minus the rest mass energy of the electron. This resulting peak is known as the single-escape peak. Similarly, if both annihilation gamma-rays escape, the only energy deposited is the kinetic energy of the electron-positron pair. This corresponding energy is the full energy of the incident gamma-ray minus twice the rest mass energy of the electron. This resulting peak is known as the double-escape peak.

Probability Statistics and Energy Resolution of a Scintillator

As described before, there exists statistical variations that causes distributions to arise for a set energy value. Therefore, we expect to see peaks with a well-defined peak and width. The peak can be assumed to follow a Gaussian distribution, given by the following empirical formulation:

$$G(E) = \frac{A}{\sqrt{2\pi}\sigma} \exp\left[\frac{-(E-E_0)^2}{2\sigma^2}\right] \tag{2}$$

where E is the energy, E_0 is the peak centroid energy, A is the area under the peak, and σ is the standard deviation of the peak.

An important measure focused on in this lab is energy resolution. Energy resolution is the measure of statistical fluctuations or noise that plague a detector, impacting accurate energy measurements. Energy resolution values close to 0 are measures of good energy resolution, signifying a peak with a thin width. The opposite case holds true for bad energy resolution. Energy resolutions can be found using the following equation:

$$R(E) = \frac{FWHM}{E_0} \tag{3}$$

where FWHM is the full width at half maximum of the peak. The FWHM can be found assuming a Gaussian distribution can be applied on the peak. This relation then results in the following standard deviation relation and energy resolution formulation:

$$FWHM = 2.35\sigma \tag{4}$$

$$R(E) = 2K\sqrt{\frac{2ln2}{E}} \tag{5}$$

where σ is the standard deviation of the Gaussian peak; K is some proportionality constant that described the linear response of a detector. While K is not known for this detector used, the energy resolution from Eq. (3) can be used to for energy resolution calculations.

Linear Attenuation and Gamma-Rays

Linear attenuation is the probability that a particle will travel a thickness of an absorber material without any interactions. These interactions are entirely dependent on the interacting particle. For gamma-rays, these interactions are coherent scattering, photoelectric effect, Compton scattering, pair production. For a given collimated beam of gamma-rays, there exists a probability that a gamma-ray does not undergo interaction with the absorber via the interactions listed before. Using these probabilities, the intensity of the collimated beam of gamma-rays as they pass through a medium is given as:

$$I(x) = I_0 e^{-\tau x} e^{-\sigma x} e^{-\kappa x} e^{-\sigma_{coh} x} = I_0 e^{-\mu x} \tag{6}$$

where $\tau, \sigma, \kappa, \sigma_{coh},$ and μ describe the linear attenuation coefficient for photoelectric effect, Compton scattering, pair production, coherent scattering, and total, respectively; and I_0 is the initial intensity.

The total linear attenuation coefficient is a measure of the number of primary gamma-rays that will have interactions per unit thickness, different from the previous discussion for the four interaction types. The components of the total linear attenuation coefficient all depend on the incoming energy of the gamma-ray and the mean atomic number of the absorbing material, Z. The mean atomic number of the absorbing material impacts what interaction occur. Photoelectric effect occurs more frequently for low-energy gamma-rays and high-Z materials. Compton scattering occurs more frequently for intermediate-energy gamma-rays and low-Z materials. Pair production events are more frequent for high-energy gamma-rays and high-Z materials. Based on the materials used and the source used, we can characterize which interaction will occur most predominantly.

Procedures

This lab consisted of conducting two experiments. The first experiment focused collecting gamma-ray energy spectra for six different gamma-ray sources using a NaI (TI) detector. The second experiment focused on obtaining energy spectra for a single source, focusing on characterizing the attenuation ability of three different materials. This section will explain each experiment conducted, focusing on what steps were taken to complete these objectives.

Experiment 1

In this experiment, we must collect the gamma-ray energy spectra for six different sources using a NaI (TI) detector. With these spectra, we'll be able to observe the desired peaks described above for each source. Furthermore, we'll be able to quantify the energy resolution of the detector used. For this experiment, we used a SOLO 00876 NaI (TI) Inorganic scintillator, a CAEN N1470AL high voltage power supply (HVPS), an ORTEC 142TH preamplifier, an ORTEC 590A amplifier, and an ORTEC Easy-MCA-2K multi-channel analyzer (MCA) The inventory number of each module is in Table 3 in Appendix A. The experimental setup is shown below:
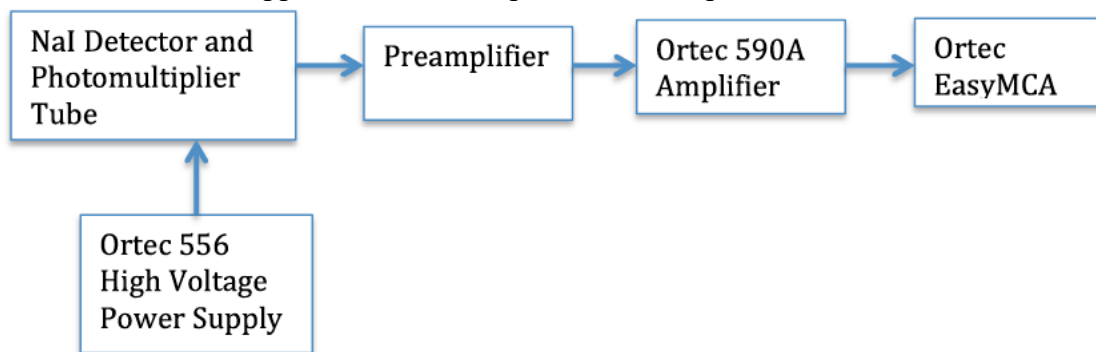

Fig. 1: Setup for Experiment 1 [1].

As mentioned before, six different sources were used for this experiment. These sources are ^{137}Cs, ^{60}Co, ^{22}Na, ^{54}Mn, ^{133}Ba, and an unknown source. Each source used had an activity of 1 μCi (September 2017). To begin, we connected the preamplifier to the amplifier. We then

connected the amplifier to the MCA and turned on the computer to use MAESTRO. The NaI (TI) detector was already connected to the preamplifier upon arriving at lab. By completing these connections, the HVPS was turned on and a positive bias of 1350 V was set on the inorganic detector.

With these parameters set, we began taking 5-min trials of each source mentioned before. The timer and the spectra were configured and collected using MAESTRO. Using the cobalt isotope, we observed that our signals on the oscilloscope were being clipped. With the help of our TA, we deduced the problem could be due to the voltage set and brought it down to 1000V. The problem persisted so the voltage was brought down to 890V. Additionally, we set a lower-level discriminator (LLD) to 20 to eliminate noise. Upon completing these tasks, we collected the spectra for all six sources. To conclude, we ran a 15-min trial to gather a spectrum for the background.

Experiment 2

In this experiment, we acquired the energy spectra for a gamma-ray source as gamma-rays traverse through varying thicknesses for three different materials. These materials are lead, iron, and aluminum. We used the same ^{137}Cs source from experiment 1. The general setup that was used in Experiment 1 is used for Experiment 2, except the configuration of the detector is changed. The configuration of the detector is shown below:
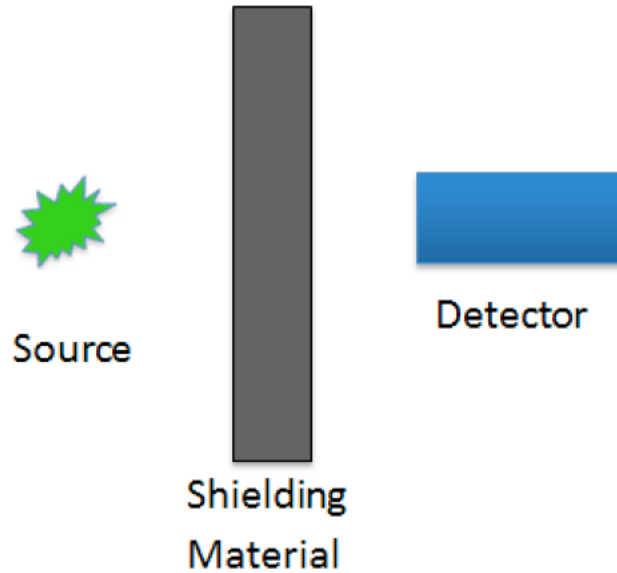
Fig. 2: Setup for Experiment 2 [1].

To begin, we ran a 5-min trial on the unattenuated source. After this collection, we began with using lead. We used five slabs of lead, each with varying thicknesses. The measured thicknesses were 25.5-mm, 25.4-mm, 25.4-mm, 25.5-mm, and 25.4-mm. The presented thicknesses occur in the order in which they were tested. We began with all five slabs and took off one slab after each 5-min spectra collection on the source.

After using lead, we used five iron slabs. The measured thicknesses of the slabs were 13.1-mm, 13.1-mm, 13.1-mm, 13.1-mm, and 13.8-mm. Again, the presented thicknesses occur in the order in which they were tested. We began with all five slabs and took off one slab after each 5-min spectra collection on the source.

After using iron, we used five aluminum slabs. The measured thicknesses of the slabs were 7.92-mm, 7.82-mm, 7.85-mm, 6.65-mm, and 6.66-mm. Again, the presented thicknesses occur in the order in which they were tested. We began with all five slabs and took off one slab after each 5-min spectra collection on the source. After concluding this collection, we turned off the HVPS and disconnected all modules.

10

Results

This section will discuss the results from each experiment, reporting numerical results explicitly. All presented plots were constructed from MAESTRO output files and Python.

Experimental Results for Experiment 1

Following the procedure outlined by Experiment 1, we collected the energy spectra for the six sources mentioned above along with a background energy spectrum. The calibration curve used only for the known sources is given below:
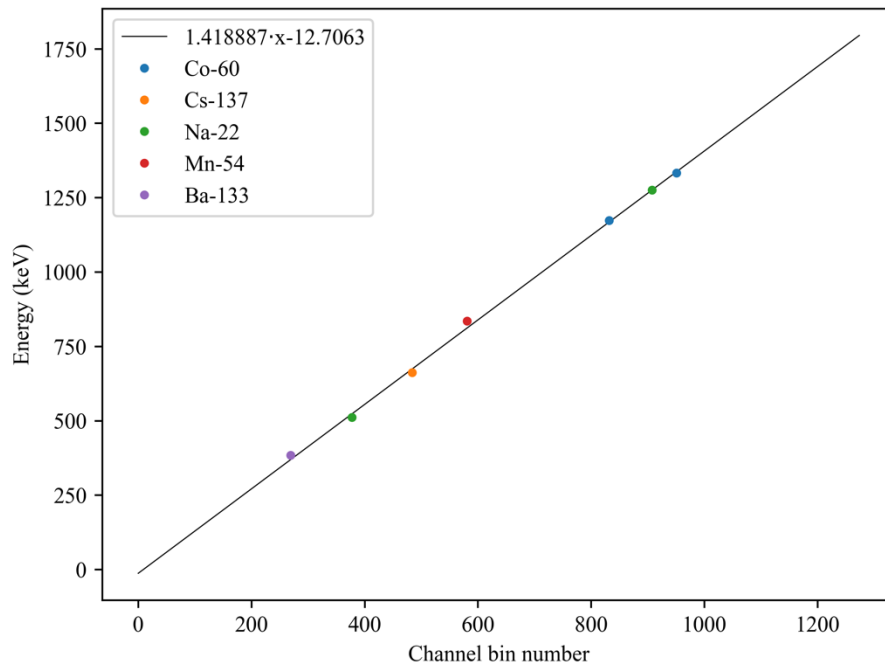

Fig. 3: Counting curve showing counts as a function of voltage for a GFPC.

Using the full-energy peaks on each spectrum, we calibrated by using the expected gamma-ray energy emitted by each source and the peak centroid channel number. However, there are four

energy peaks for the barium isotope that must be used for calibration. However, we omit the 276, 303, and 384 keV peaks because we decided that we have enough peaks to conduct an accurate calibration on the detector. To continue, we used a line regression fit function in Python to get the calibration coefficient. Table 1 gives the expected gamma-ray energy and peak centroid channel number used for said calibration:

Table 1: Expected gamma-ray energy used for calibration.

Gamma Source	Energy (keV)	Peak Centroid Channel Number
^{60}Co	1173, 1333	832, 951
^{137}Cs	661.7	484
^{22}Na	511, 1275	377, 908
^{54}Mn	835	581
^{133}Ba	356	269

It's important to note we did not use the spectra for the unknown source and background since we must discern the isotopes that compose these spectra. Using a fit function in Python, we found a calibration coefficient of 1.42 keV bin^{-1} that could be applied to all used to calibrate all acquired spectra. The calibrated spectra for the measured sources along with the unknown source and background source are shown below:
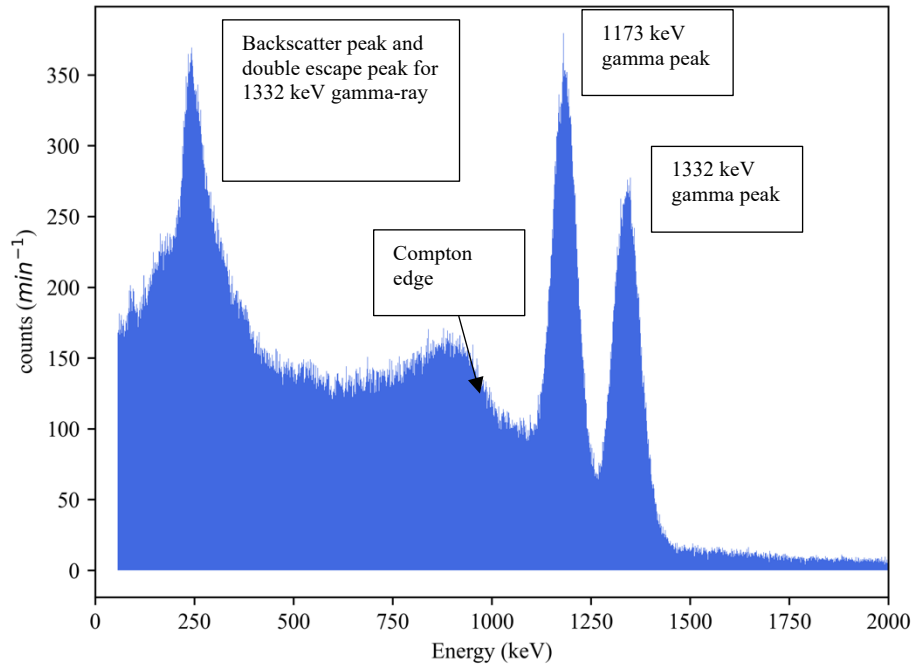
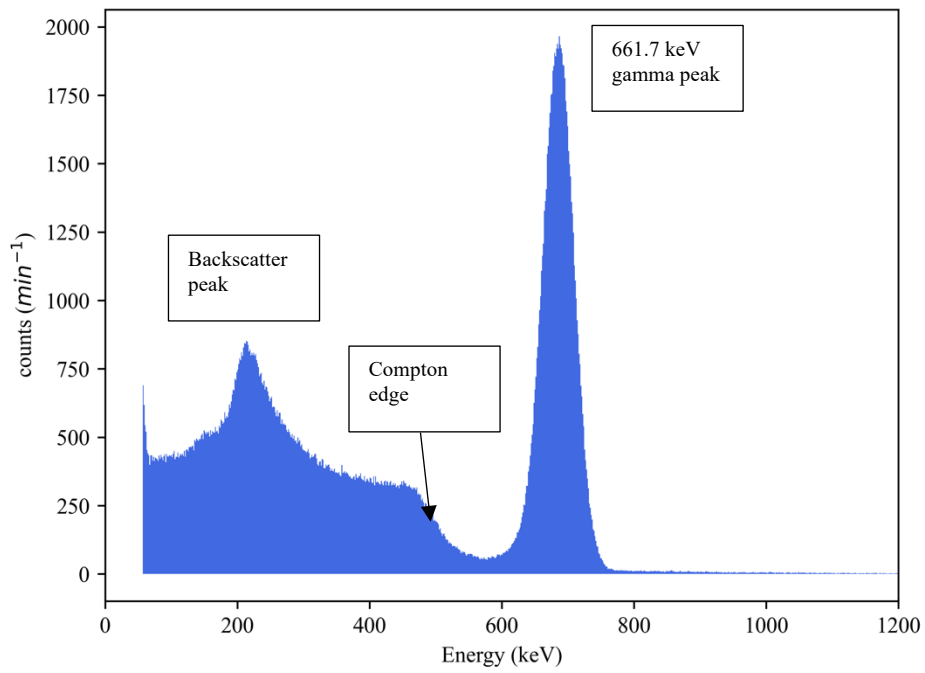Fig. 4: Calibrated spectrum for cobalt isotope used.

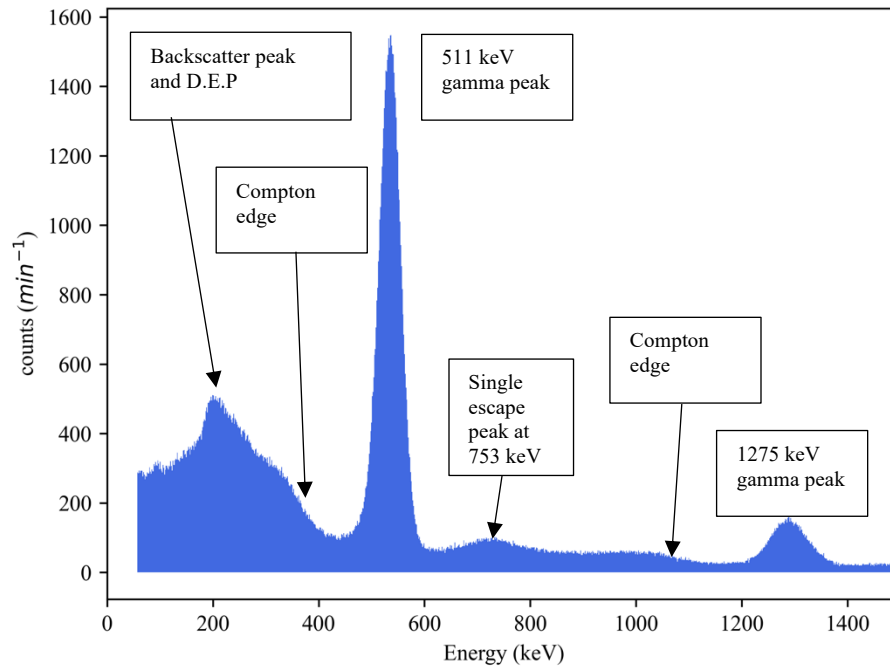Fig. 5: Calibrated spectrum for cesium isotope used.

Fig. 6: Calibrated spectrum for sodium isotope used.
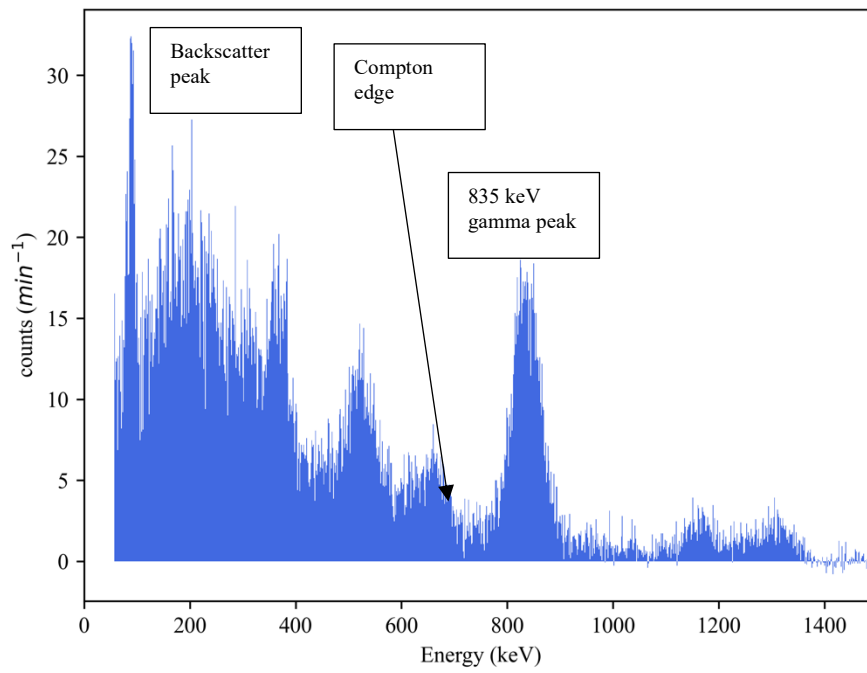

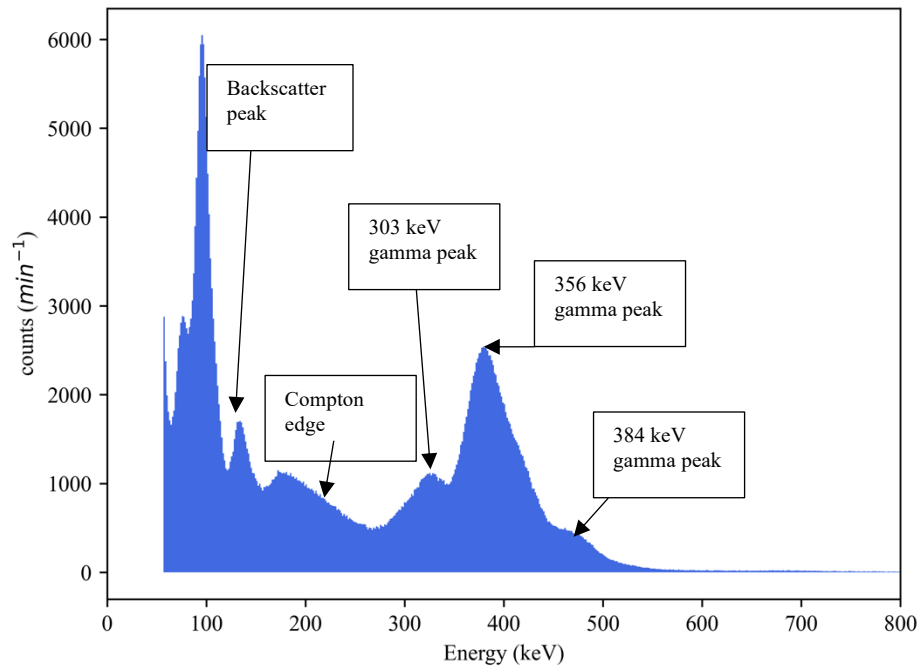Fig. 7: Calibrated spectrum for manganese isotope used.

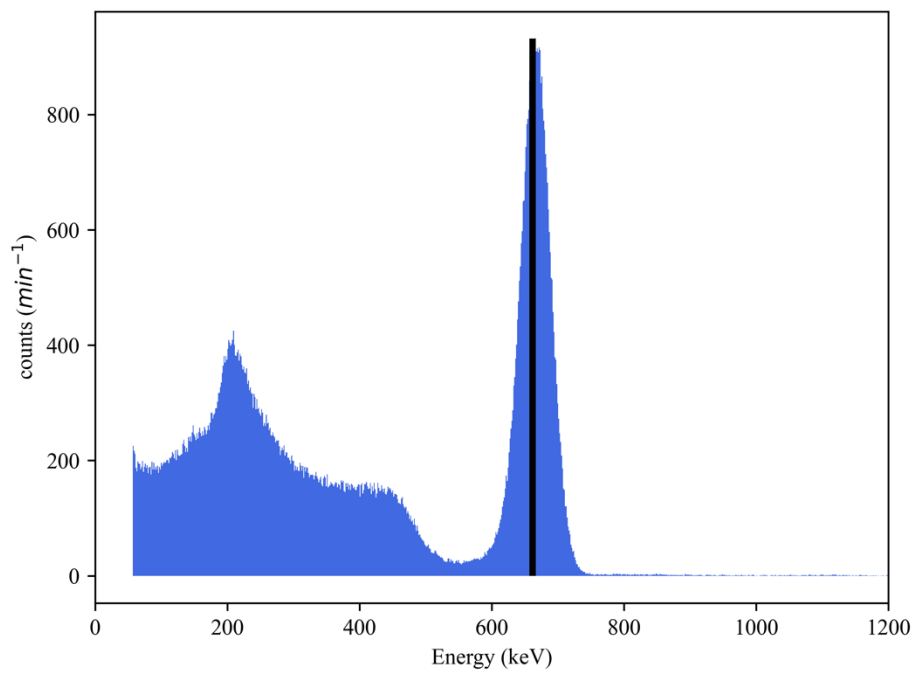Fig. 8: Calibrated spectrum for barium isotope used.

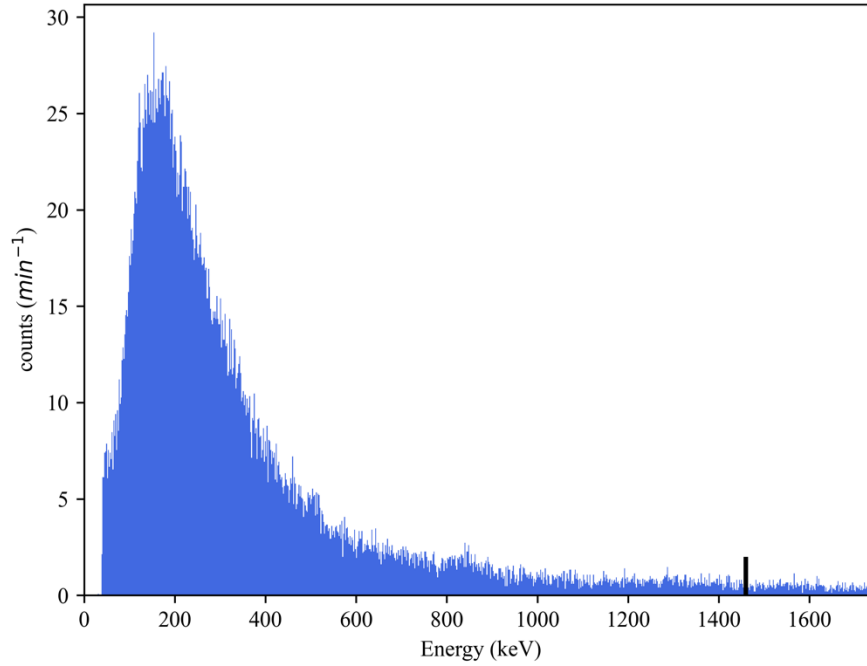Fig. 9: Calibrated spectrum for unknown source used.

Fig. 10: Calibrated spectrum for background.

Figures 9 and 10 contain sources of unknown identity. We deduced the unknown source in Fig. 9 to be ^{137}Cs. The unknown makeup of the isotopes in the energy spectra in Fig. 10 is ^{40}K. The reasoning behind this deduction will be explained in the Discussion section. With these plots shown, we then plotted counts against energy for the identified full-energy gamma peaks for each known source used. This result is shown below:
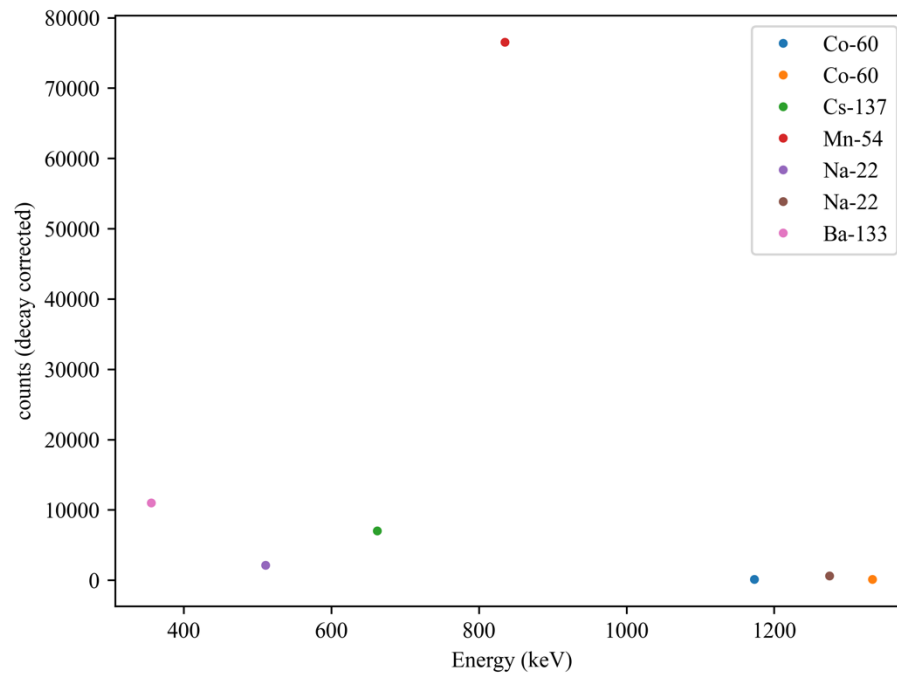
Fig. 11: Counts (decay-corrected) as a function of energy for identified full-energy gamma peaks.

However, the manganese isotope is a clear outlier from our data processing, so we opted

to show a version of Fig. 11 to clearly show the trend needed for explanation:
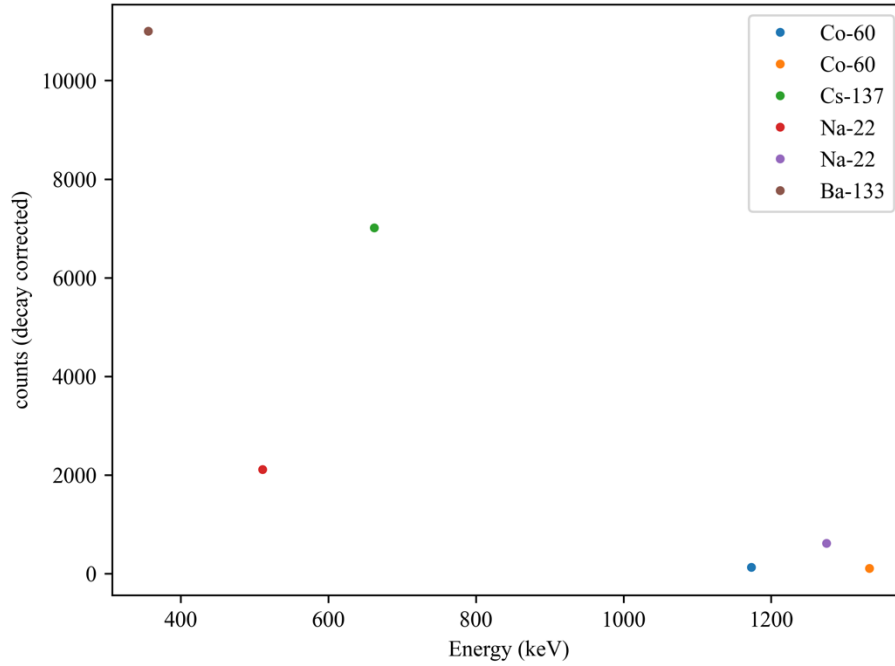
Fig. 11: Counts (decay-corrected) as a function of energy for identified full-energy gamma peaks.

We formulated Figures 11 and 12 by taking the acquired energy spectrum for each source and summing the counts under the defined peak used for calibration. For this deliverable, we omit again the 276, 303, and 384 keV gamma-ray peaks for the barium isotope due to difficulty arising in discerning the counts under the corresponding peaks. To find the counts under these peaks, we planned to use a Gaussian fit function on each peak. This fit would allow us to find the number of counts under each peak and be used to update the trend shown in Fig. 11 and Fig. 12. An illustration of this method is shown below:
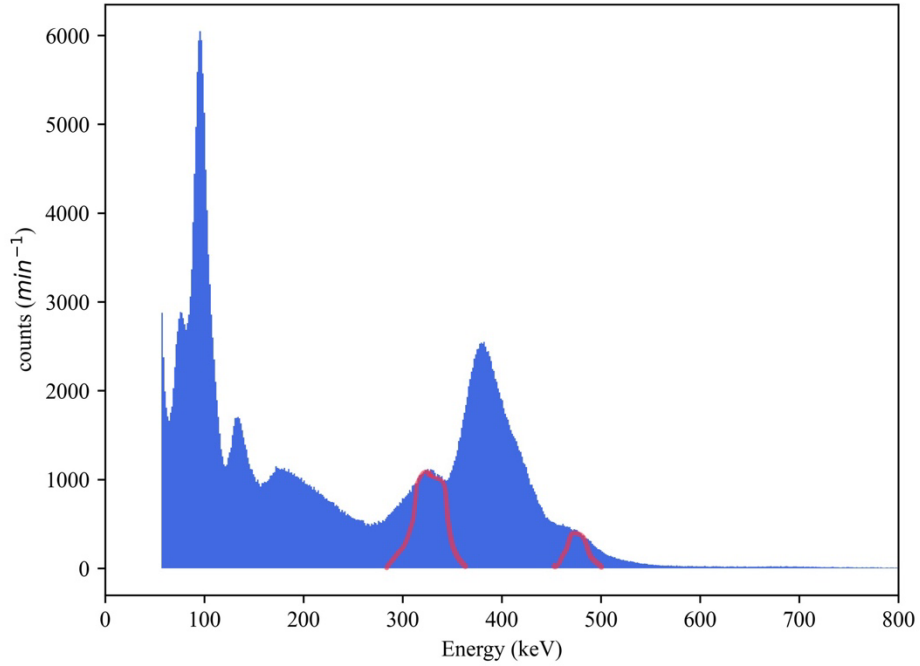
Fig. 13: Gaussian fit procedure for the unused barium gamma-ray peaks.

Additionally, the peak corresponding to 276 keV would fall within range of the 303 keV peak so we decided to omit this peak from Fig. 13. Therefore, the 356 keV peak is the only peak shown above. To accurately determine the number of counts under this peak, we had to ignore a specific section of counts to accurately find the correct number of counts. The section we opted to ignore is shown in the following illustration:

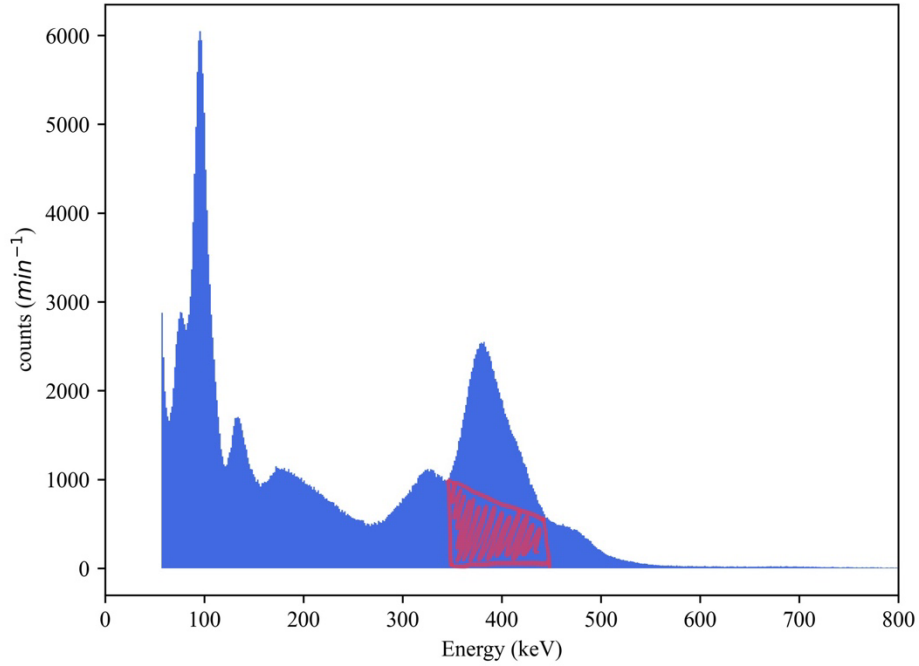Fig. 14: Ignored section of counts used to find the counts under peak.

It's important to note that the two methods described before would've and were used for the barium isotope only. Additionally, we had to compare different sources with different activities and branching ratios. By correcting the counts by the decay of the source since the time of its creation, we could accurately compare counts as a function of energy. We corrected our counts by taking the exponential component of the radioactive decay law and dividing the summed counts by this factor. Furthermore, we tabulated peak centroid energy, errors associated with these energies, expected peak energy, standard deviation, and FWHM for all peaks used in calibration. These results are presented below:

Table 2: Tabulated PCE, error, expected peak energy, standard deviation, and FWHM for peaks used in calibration.

Isotopes	Peak Centroid Energy (PCE) (keV)	Error Associated with PCE	Expected Peak Energy (keV)	Standard Deviation (keV)	FWHM
^{60}Co	1180.5	16.7%	1173	33.2	78.1
^{60}Co	1349.4	18.3%	1333	35.1	82.3
^{137}Cs	686.7	12.7%	661.7	23.5	55.3
^{54}Mn	824.4	13.7%	835	23.7	55.6

^{22}Na	535.6	11.8%	511	21.5	49.7
^{22}Na	1288.4	17.7%	1275	36.8	86.6
^{133}Ba	381.681	11%	384	27.8	65.3

We found the PCE and FWHM by parsing through the MAESTRO files for each respective energy spectra. The error associated with PCE was found through using error propagation on the line regression fit function as described above. Finally, the standard deviation of each peak was found by using Eq. (4) and the peak centroid energy. A sample calculation for the first peak for the cobalt isotope is shown below:

$$\sigma = \frac{78.1}{2.35} = 33.2 \ keV$$

The same process was applied for the standard deviation shown in Table 2.

With important statistical parameters regarding our spectra defined, we can now form an understanding of the energy resolution in using an inorganic scintillator. We can plot energy resolution as function of the natural log of energy to see how the energy resolution changes as the energy of the incoming gamma-ray increases. This result is shown below:
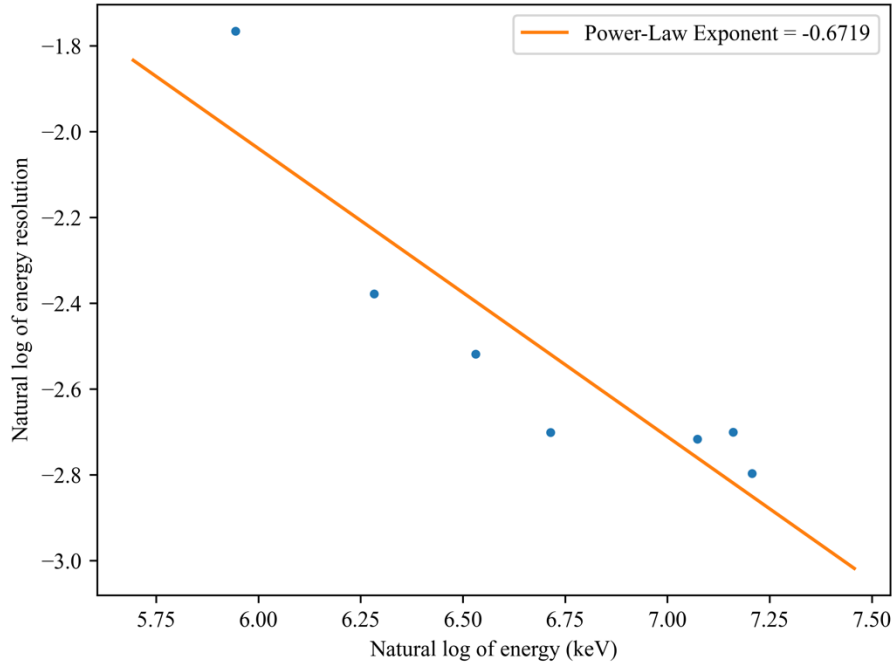
Fig. 15: Energy resolution as a function of energy.

Experimental Results for Experiment 2

Following the experimental procedure detailed in Experiment 2, we measured the linear attenuation coefficients (LACs) of gamma-rays for lead, iron, and aluminum using an inorganic scintillator. We'll compare these experimental values to values found in literature to garner a sense of the feasibility of using such detectors for these types of measurements.

To find the LAC for each material tested, we must determine a region of interest (ROI) that contains the highest energy peak corresponding to the full energy of the emitted gamma from the cesium source mentioned above. This ROI is kept constant as the thickness of each material tested is increased. Before presenting the experimental LAC measured, the expected LAC values are tabulated below:

Table 3: Expected LAC for the materials tested [2].

Material	LAC (cm^{-1})
Lead	1.4152
Iron	0.2107
Aluminum	0.6066

We found the mass attenuation coefficients values using Reference [2] and interpolated using a gamma-ray energy of 661.7 keV. Furthermore, we took the density of each material listed above and multiplied by the mass attenuation coefficient to find each LAC. With the expected LAC values found, we can use the ROI to find the number of counts under the ROI peaks. Specifically, we'll take the natural log of these counts and find the associated error using error propagation. The natural log of ROI counts and their associated error are tabulated below for each material:

Table 4: ROI counts and associated error for lead.

Thickness of lead (mm)	Natural log of ROI counts	Associated error
25.5	8.810	0.0122
25.4	8.193	0.0166
25.4	7.590	0.0225
25.5	7.059	0.0293
25.4	6.719	0.0347

Table 5: ROI counts and associated error for iron.

Thickness of iron (mm)	Natural log of ROI counts	Associated error
13.1	8.805	0.0122
13.1	8.139	0.0171
13.1	7.573	0.0227
13.1	7.035	0.0296
13.8	6.677	0.0355

Table 6: ROI counts and associated error for aluminum.

Thickness of aluminum (mm)	Natural log of ROI counts	Associated error

7.92	9.049	0.0108
7.82	8.635	0.0133
7.85	8.214	0.0165
6.65	7.850	0.0197
6.66	7.501	0.0235

With these values tabulated, we can plot the natural log of ROI counts against thickness for each material. These plots are shown below:
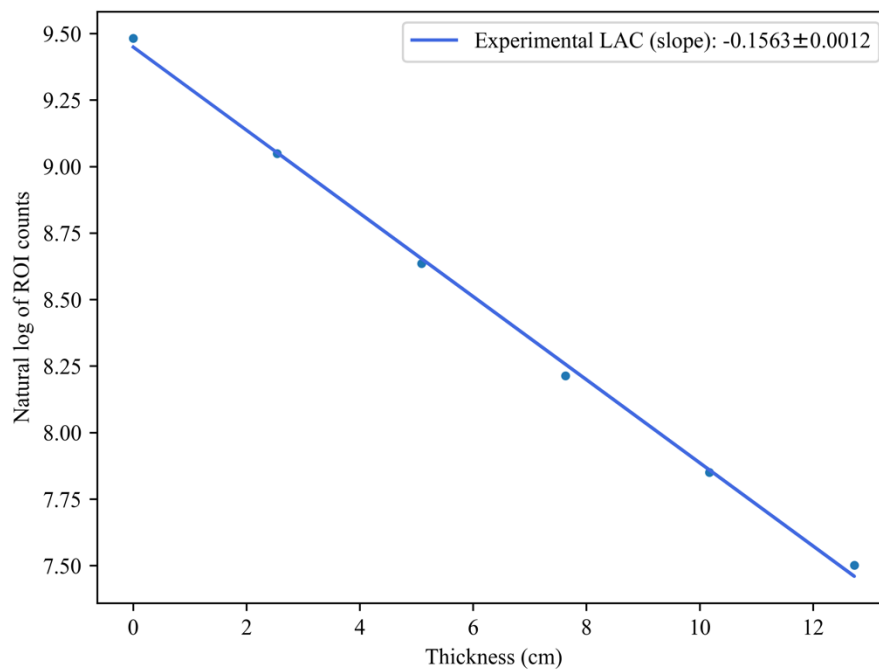

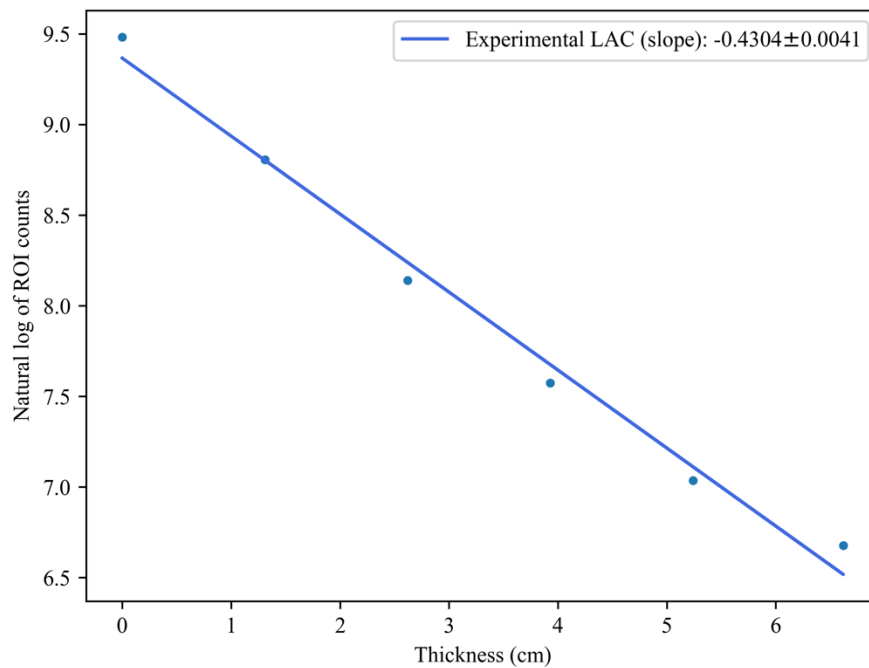Fig. 16: Natural log of ROI counts as a function of thickness for lead.

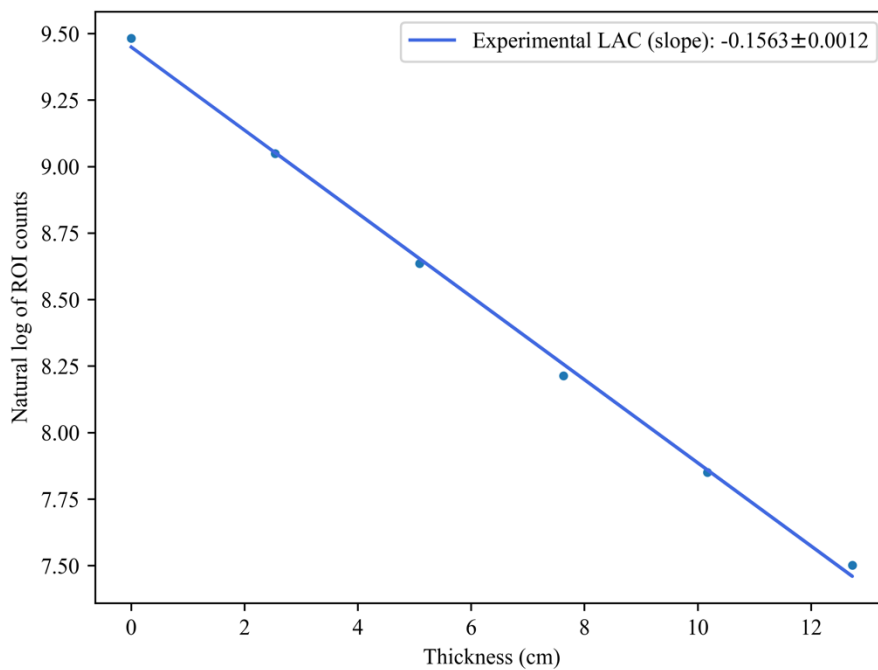Fig. 17: Natural log of ROI counts as a function of thickness for iron.

Fig. 18: Natural log of ROI counts as a function of thickness for aluminum.

For Figures 16-18, we can find the experimental LAC for each material tested by finding the slope of linear line shown above. Furthermore, the associated error with this measurement is also provided. Both the experimental LAC values and associated errors were found using a linear fit function on Python. With these values, we can then compare both experimental and expected values and deduce whether the detector used is a viable method of determining LACs for different materials.

Discussions

The validity of the results and any potential sources of error for all experiments will be thoroughly examined.

Discussions for Experiment 1

error

Discussions for Experiment 2

The

Discussions for Experiment 3

The

Conclusions

In

References

[1] Di Fulvio, A., & Romanchek, G. (2023, August 15). *NPRE 451 Fall 2023 Lab Manual* [Review of *NPRE 451 Fall 2023 Lab Manual*].

https://canvas.illinois.edu/courses/43494/files/11034313?module_item_id=3089940

Appendix

Appendix A: Instrumentation Specifications

Table 1: Instruments specific information.

Module	Manufacturer	Model Number	Inventory #
Multi-Channel Analyzer	ORTEC	Easy-MCA-2K	P10F79090
Gas Flow Proportional Counter	LND, INC.	4911	N/A
High Voltage Power Supply	CAEN	N1470AL	P10G96071
Preamplifier	ORTEC	142TH	C75656
Amplifier	ORTEC	590A	N/A
Timer/Counter	ORTEC	871	N/A
NIM	ORTEC	4001A	C83249
Oscilloscope	Tektronix	TBS1102C	P10H00528